Archives of Mining Sciences **52**, Issue 1 (2007) 3–20

TAE HYUNG KIM*, ERWINSYAH PUTRA*[1], DAVID S. SCHECHTER*

ANALYZING TENSLEEP NATURAL FRACTURE PROPERTIES USING X-RAY CT SCANNER

ANALIZA WŁASNOŚCI SZCZELIN NATURALNEGO ZŁOŻA "TENSLEEP" PRZY UŻYCIU SKANERA RENTGENOWSKIEGO (X-RAY CT)

This paper presents a step by step to characterize fracture properties of Tensleep formation cores using X-ray CT Scanner. Two cores from the RMOTC 48X28 well at Teapot Dome field were used as an example. The fracture aperture, fracture aperture distribution and mineralization condition of both cores are analyzed and compared. The CT scanner provides CT images, which show the difference between material densities. These images are not the actual physical property of fracture. The technique to convert the CT images into aperture size is presented.

Keywords: CT scanning, fracture apperture, core analyse, reservoir heterogenity

Niniejszy artykuł opisuje krok po kroku sposób badania własności szczelinowatych utworów Tensleep z wykorzystaniem skanera tomografii komputerowej. Dwa rdzenie pobrane z otwory RMOTC 48X28 ze złoża Teapot Dome pokazane zostały przykładowo. Rozwarcie szczelin, rozkład rozwarcia szczelin oraz warunki mineralizacji obu rdzeni zostały przeanalizowane i porównane. Tomograf CT pozwala na uzyskanie obrazów CT na których jest możliwa analiza różnicy gęstości materiałów. Jednakże takie obrazy nie oddają aktualnego stanu własności szczeliny. Specjalna technika konwersji tych obrazów CT umożliwiająca określenie stanu rozwarcia szczelin została pokazana w artykule.

Słowa kluczowe: skanowanie tomografem CT, rozwarcie szczeliny, analiza rdzenia, niejednorodność złoża

* PETROLEUM ENGINEERING DEPARTMENT, TEXAS A&M UNIVERSITY, TEXAS, USA
http://pumpjack.tamu.edu/Faculty&Staff/faculty/schechter/baervan/homepage.html
* THESE AUTHORS CONTRIBUTED EQUALLY TO THIS WORK
[1] CORRESPONDING AUTHOR
E-MAIL ADDRESSES: TK: rokguy@tamu.edu; EP: putra@tamu.edu; DSS: david.schechter@pe.tamu.edu

1. Introduction

The structure of the Teapot Dome is an elongated anticline, striking NNW-SSE, probably produced by a reverse fault whose strike is also NNW-SSE, and is located in the southwestern part of the anticline (Fig. 1)(Putra et al., 2004). This reverse fault is dipping roughly to the NE and is considered the main fault. There are also three small faults that represent accommodation faults produced after the movement of the main fault. Most fractures generally terminate vertically at bedding planes and stylolites.

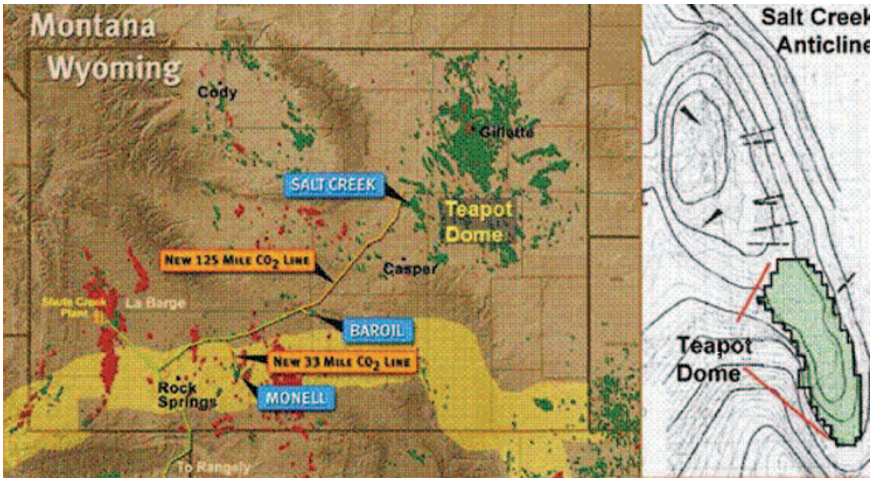

Fig. 1. Teapot Dome, NE Natrona Co., central Wyo., 30 mi/48 km NNE of Casper, WY. The teapot-shaped rock formation is also shown (Putra et al., 2004)

Rys. 1. Położenie złoża Teapot Dome, NE Natrona Co., central Wyo., 48 km NNE od miejscowości Casper, WY. Pokazano również formację Teapot (Putra et al., 2004)

The Tensleep sandstone is observed to be heavily fractured (Fig. 2). Most of the fractures are less than a millimeter in total width, and much of that width is occluded in the smaller fractures by partial mineralization of quartz and/or dolomite. Nevertheless significant porosity in the range of 10-80% remains in most fractures especially within the larger ones (Lorenz & Cooper, 2004). The larger fractures also typically split the rock and core is no longer intact across the fracture plane indicating that mineralization provides only an incomplete and weak seal between fracture faces. A zone of inclined fractures is present between 5591 ft and 5595 ft and these fractures are suggestive of a conjugate shear system similar to that seen in Tensleep outcrops immediately south of the Alcova reservoir (Lorenz & Cooper, 2004). A short of interval of white, micritic dolomite with numerous bitumen-stained natural fractures is present between 5495 and 5498 ft overlying the oil-saturated reservoir facies (Lorenz & Cooper, 2004).

a)

b)

Fig. 2. Cores from Tensleep formation: a – A natural fracture face that is partially covered with crystalline dolomite, b – Highly fractured Tensleep sandstone (Lorenz & Cooper, 2004)

Rys. 2. Rdzenie z utworów formacji Tensleep: a – wnętrze naturalnej szczeliny jest częściowo pokryte kryształami dolomitu, b – silnie zeszczelinowany piaskowiec Tensleep (Lorenz & Cooper, 2004)

The main objective of this paper is to characterize the Tensleep rock currently operated by the Rocky Mountain Oilfield Testing Center (RMOTC). As shown by recent core analysis, the Tensleep Formation in Teapot Dome is heavily fractured and the reservoir is considered as a good candidate for CO_2 sequestration. For the success of CO_2 sequestration, it is crucial to know the characteristics of fractures. Using 4^{th} generation X-Ray tomography unit (CT scanner), fracture properties such as fracture aperture, fracture aperture distribution and mineralization are obtained without damaging the core.

2. Experimental Procedures

Fractures of two cores recovered from RMOTC 48X28 well were characterized with CT scanner which allows fracture characterization without damaging cores. The X-Ray CT scanner is a Universal Systems HD-350E (Fig. 3).

Fig. 3. Universal Systems HD-350E

Rys. 3. Uniwersalny układ pomiarowy HD-350E

It is able to scan as fast as 1 sec/scan and has 75 cm diameter gantry. It can analyze a core plug up to 81 cm long and gives a spatial resolution of 0.35 mm (Universal Systems Website). However; the data that we analyzed are raw pixel data rather than the spatial data from CT image. If CT images (digital images) are analyzed directly to calculate aperture, accuracy of 0.35 mm spatial resolution will be questionable. According to Shannon's sampling theorem, the digitizing device must utilize a sampling interval that is no greater than one-half size of the smallest resolvable feature of the optic image. Thus, sampling should be done less than 175 μm for 0.35 mm spatial resolution. X-Ray CT Scanner oversamples and oversampled data provide extra pixels that do not theoretically contribute to the spatial resolution, thus they can improve the accuracy of the scan feature and aperture size smaller than a spatial resolution is able to be calculated. In order to characterize Tensleep rock the procedures of the experiment are as follows:

1) Artificially cut the core
2) Use different known feeler sizes to develop calibration curve for Tensleep sandstone and then use calibration curve to convert CT number into fracture aperture size.
3) Develop matrix calibration curves to compensate the beam hardening effect.
4) Take CT images of Core-A and Core-B
5) Use the calibration curve to obtain fracture aperture size and generate fracture aperture contour maps.

Details of the calibration curve, CT scanning and analysis of the fracture aperture using log normal density function are described below.

2.1. Calibration Curve

X-ray CT scanner identifies the density differences between various objects (Wellington & Vinegar, 1985). The density of a fracture that is filled with air is less than the density of the rock matrix. Thus CT images can differentiate between matrix and fracture. The CT numbers do not represent aperture size of the fracture as they are mere functions of densities. In order to obtain the fracture aperture, a calibration technique has to be applied to correlate the CT numbers with the actual aperture size (Muralidharan et al., 2004a, 2004b).

The experimental setup consists of two halves of a rock specimen, feeler gauges and a core holder. The rock specimen was obtained from unfractured part of a Tensleep core. Then it was cut using a diamond saw along the longitudinal direction. Cut faces were grinded using a grinding machine to reduce surface roughness as much as possible. Smooth faces ensure a proper match between the halves so that an accurate small fracture aperture can be obtained. Feeler gauges of known sizes were then inserted between the halves (Fig. 4). The following sizes of feeler gauges were used in the calibration experiment: 51 μm, 76μm, 20 μm, 279 μm, 330 μm.

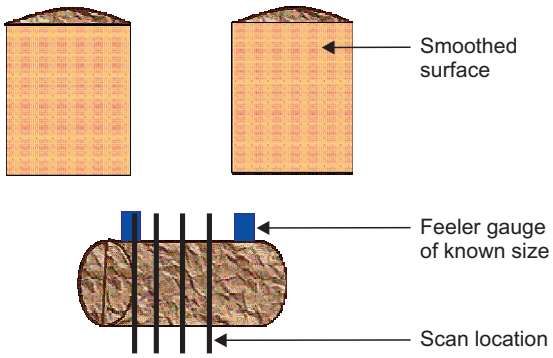

Fig. 4. Schematic view of feeler gauge locations and scanning locations (Muralidharan et al., 2004a)

Rys. 4. Widok schematyczny położenia szczelinomierza (*feeler gauge*) i położenia obszaru skanowania (Muralidharan et al., 2004a)

The feeler gauge inserted in the core was placed in the core holder and 500 psi overburden pressure was applied. Multiple CT scans were taken in the middle of the core between the two feeler gauges along the longitudinal direction. Fig. 5 shows typical sets of scans of a Tensleep core with various feeler gauges. The more dense area is shown with an orange color and less dense area is shown green, blue and black in decreasing order of density. The feeler gauge is made from the steel therefore the density of this material is very high. The feeler gauges were placed at the both ends and some images were affected by these gauges if CT scan were taken close to these gauges, which usually referred to as beam

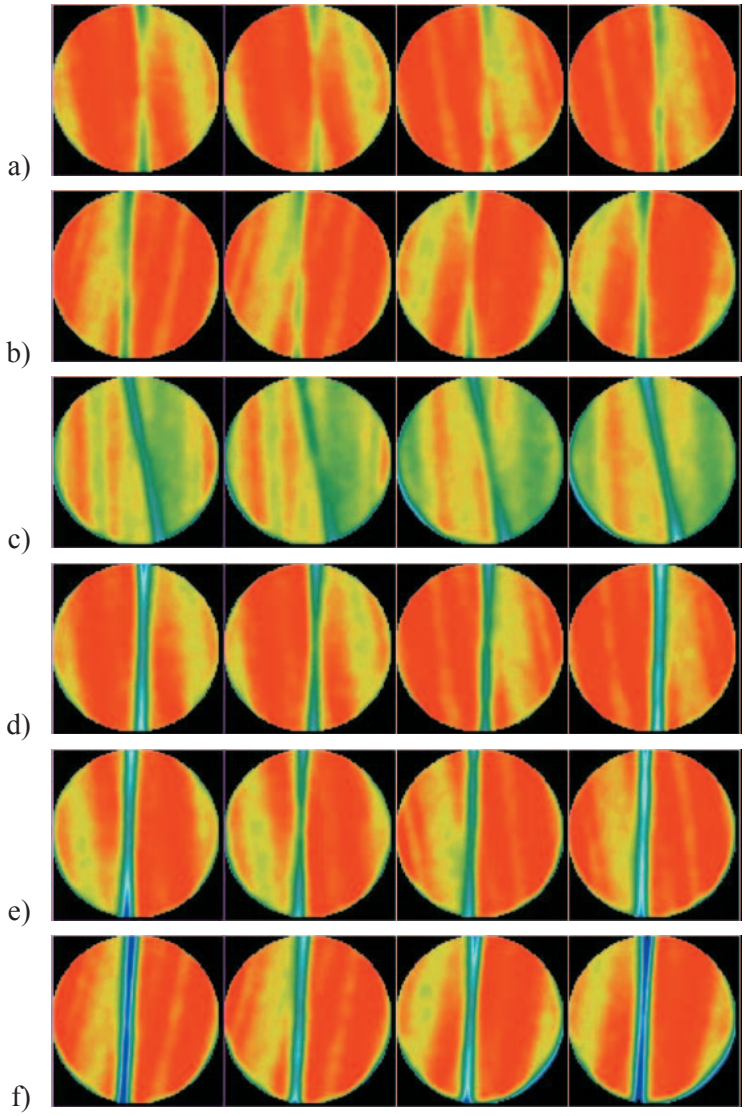

Fig. 5. Scanning images with various feeler gauge sizes: a – 51 μm feeler gauge, b – 76 μm feeler gauge, c – 127 μm feeler gauge, d – 203 μm feeler gauge, e – 279 μm feeler gauge, f – 330 μm feeler gauge

Rys. 5. Obrazy ze skanera z różnymi rozwartościami szczelinomierza (*feeler gauge*); szczelinomierz o grubości: a – 51 μm, b – 76 μm, c – 127 μm, d – 203 μm, e – 279 μm, f – 330 μm

hardening effect. The affected CT images can be identified by the slightly bent images. These images were not used in calibration calculation. Fig. 6 is an example of CT number plot for 203 μm fracture size. Horizontal lines represent rock matrix and a dip of a CT number in the middle of the plot represents fracture. Although the matrix and the fracture

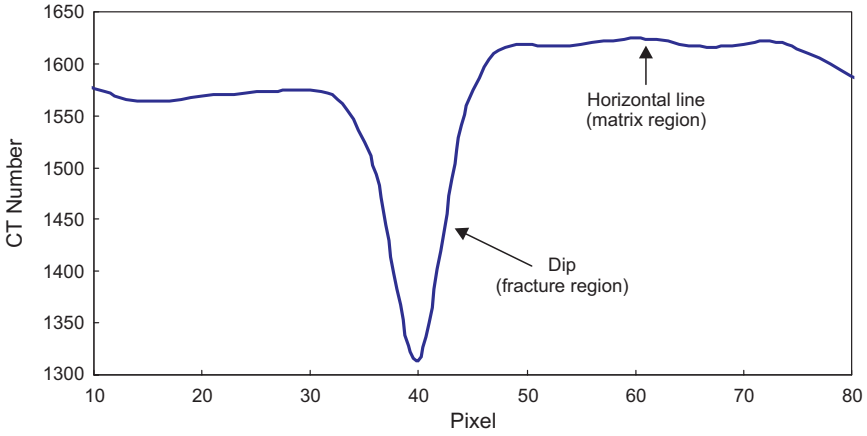

Fig. 6. Average CT number plot of 203 μm feeler gauge

Rys. 6. Wykres wynikowy na podstawie skanowania CT dla szczelinomierza o grubości 203 μm

can be clearly distinguished with CT number, it is impossible to determine the aperture size with CT number only. However, this CT numbers correspond to the known fracture size of 203 μm. Thus the aperture size can be calculated using this relationship. The dip of the CT number plot due to fracture is not abrupt, but rather has a smooth transition from matrix to fracture. This effect is due to dispersion of CT numbers caused by the finite beam width and oversampling. Fig. 7 shows CT number plots for different feeler gauge sizes. We found that if the feeler gauge size increases the CT numbers of fracture

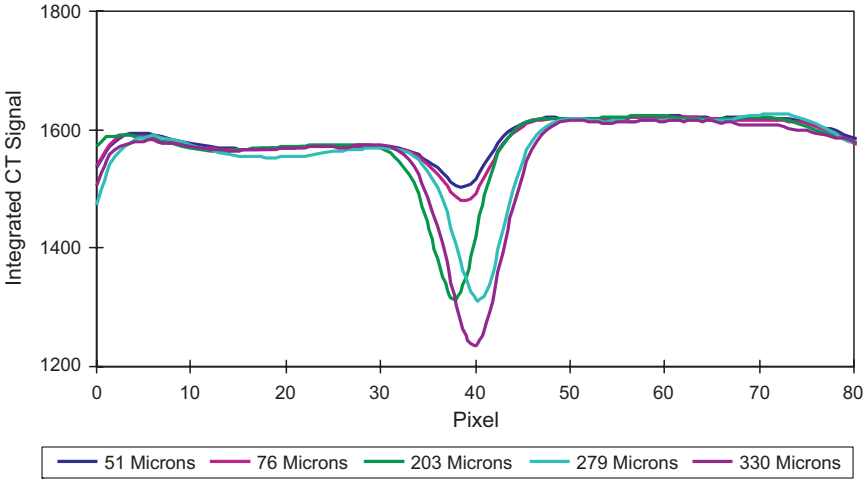

Fig. 7. Comparison of CT number plots for various fracture size

Rys. 7. Porównanie wykresów wynikowych CT dla różnych wielkości szczelin

decrease and thus the dip of CT numbers is deepened and widen. As mentioned earlier, the CT number difference is due to density difference. The CT number of fracture filled with air would be expected to have similar CT number to the air. It is true for large void space but not for a narrow space like rock fracture. CT number of fracture is affected by surrounding rock and it is usually called "oversampling" (Muralidharan et al., 2004a).

A plot of CT number was made based on the CT numbers obtained from each scan. An average CT number plot was obtained to account for minor variation in fracture size and matrix heterogeneity. Fig. 8 is an example of an average CT number plot. From an average CT number plot, minimum rock CT number is identified. All CT numbers those are smaller than the minimum rock CT number are subtracted from the minimum rock CT number and the differences are used to obtain the integrated CT signal for the fracture size. The integrated CT signals are calculated for each pixel number and are given indexes starting from 1 to n as shown in Fig. 8. The area of integrated CT region is calculated using the following formula (Muralidharan et al., 2004a, 2004b):

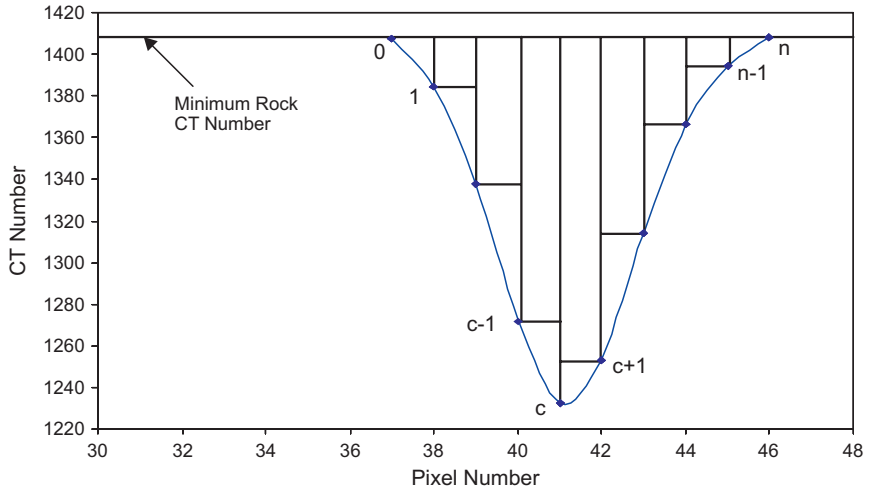

Fig. 8. Integrated area of fracture region (Muralidharan et al., 2004a)

Rys. 8. Obliczana metodą całkowania powierzchnia przekroju szczeliny

For index i equals to 1 to c,

$$Area(i) = IntCT(i-1) + \frac{1}{2}[IntCT(i) - IntCT(i-1)] \tag{1}$$

For index i equals to $c + 1$ to n,

$$Area(i) = IntCT(i) + \frac{1}{2}[IntCT(i-1) - IntCT(i)] \tag{2}$$

After calculating areas for different feeler gauges, plots of integrated CT signal versus aperture size shows a linear relationship as it can be seen in Fig. 9. The correlation of aperture size derived from this calibration curve is expressed by the following formula.

$$Fracture\ \ Aperture = \frac{IntCT - 360.99}{6.5458} \tag{3}$$

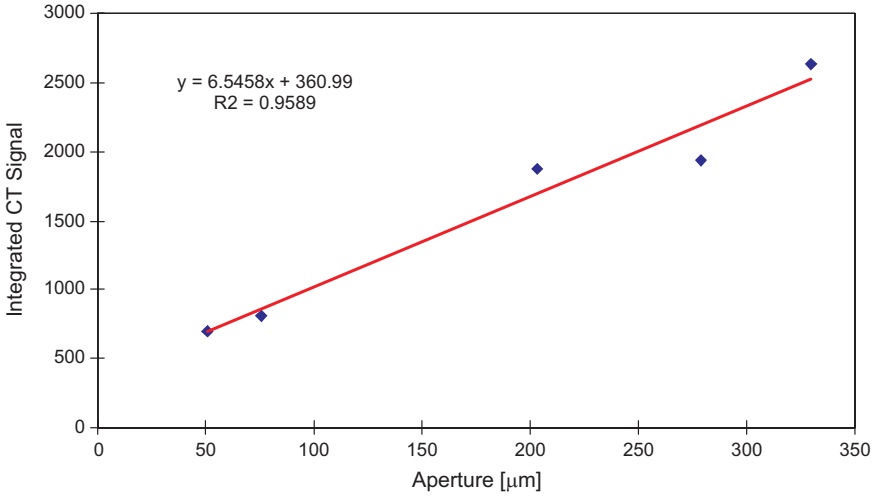

Fig. 9. Calibration between Integrated CT Signal and Fracture Aperture

Rys. 9. Kalibracja sygnału zintegrowanego CT oraz wielkości rozwarcia szczeliny

2.2. CT Scanning

The cores scanned were retrieved from depth between 5565 ft (Core-A) and 5566 ft (Core-B). Diameter of both cores is 2.52 inch and the length of Core-A and Core-B is 5.55 inch and 7.64 inch, respectively. CT images of the cores were taken under no overburden pressure condition.

2.3. Log-normal distribution

Once the cores were scanned, the results were converted to fracture aperture maps. Then, we determine the fracture aperture distribution using log normal density function. It is well known that aperture distribution follows log-normal distribution (Muralidharan et al., 2004a, 2004b). A random variable x has a log-normal probability distribution if $\ln x$ is normal. In this case, the density function of x is expressed as followed (Ang & Tang, 1975).

$$f(x) = \frac{1}{\sqrt{2\pi}\varsigma} \mathrm{Exp}\left[-\frac{1}{2}\left(\frac{\ln x - \lambda}{\varsigma}\right)^2\right] \quad 0 \le x < \infty \tag{4}$$

where,

$$\lambda = \ln \mu - \frac{1}{2}\varsigma^2 \tag{5}$$

$$\varsigma^2 = \ln\left(1 + \frac{\sigma^2}{\mu^2}\right) \tag{6}$$

μ and σ represent mean and standard deviation of a random variable x, respectively.

3. Results and Discussions

CT images of two cores were taken. The depth of Core-A and Core-B is 5565 ft and 5566 ft, respectively (Fig. 10). A total 30 scans were taken for Core-A as well as 15 images contained the information of fracture (Fig. 11). For Core-B, 17 images contained fracture among a total 50 scans were taken (Fig. 12). Figs. 13 and 14 show single CT image of Core-A and combination of multiple images that form a 3-D image of Core-A.

a)

b)

Fig. 10. Measured cores from Tensleep Formation. a – Core-A, b – Core-B

Rys. 10. Badane rdzenie z utworów formacji Tensleep. a – rdzeń A, b – rdzeń B

Fig. 11 reveals that the fracture of Core-A is not extended to the outside of the core. Mineral does not precipitate inside of the fracture. The CT images also show a large void space that is seen as a cloud like shape and the open fracture looks like a board in 3D imaging (Fig. 14). The upper part of the CT images shows mineralized fractures that have red or orange colors as observed in Fig. 13. Core-B shows a set of open fractures and a set of mineralized fractures. As discussed in core analysis, Core-B fractures were precipitated with highly dense minerals like dolomite (Figs. 12 and 15). Mineralized fractures are extended to the outside of the core. These fractures are parallel then join together. The open fracture is also extended to the side of the core and terminated by the mineralized fracture (Fig. 15). It seems that the open fracture was secondary set or caused by drilling induced fracture. Fig. 16 shows a 3-D image of the open fracture.

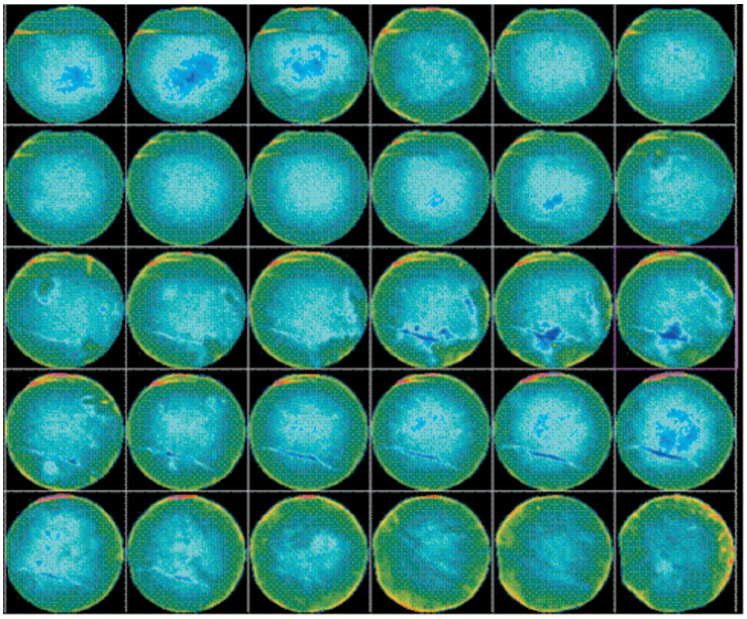

Fig. 11. CT images of Core-A

Rys. 11. Obrazy CT z rdzenia A

As mentioned earlier, a minimum rock CT number is required to determine the aperture size of a fracture. In order to get a proper value, the minimum rock CT number is taken based on the function of pixel position as shown in Fig. 17. This figure shows that different CT numbers present at different pixel position in the core. Once the minimum CT numbers were obtained the area below the minimum CT line were calculated. All the CT images were then analyzed and the fracture distribution obtained was plotted in distribution function (Fig. 18). Using mean and standard deviation following Equation 4,

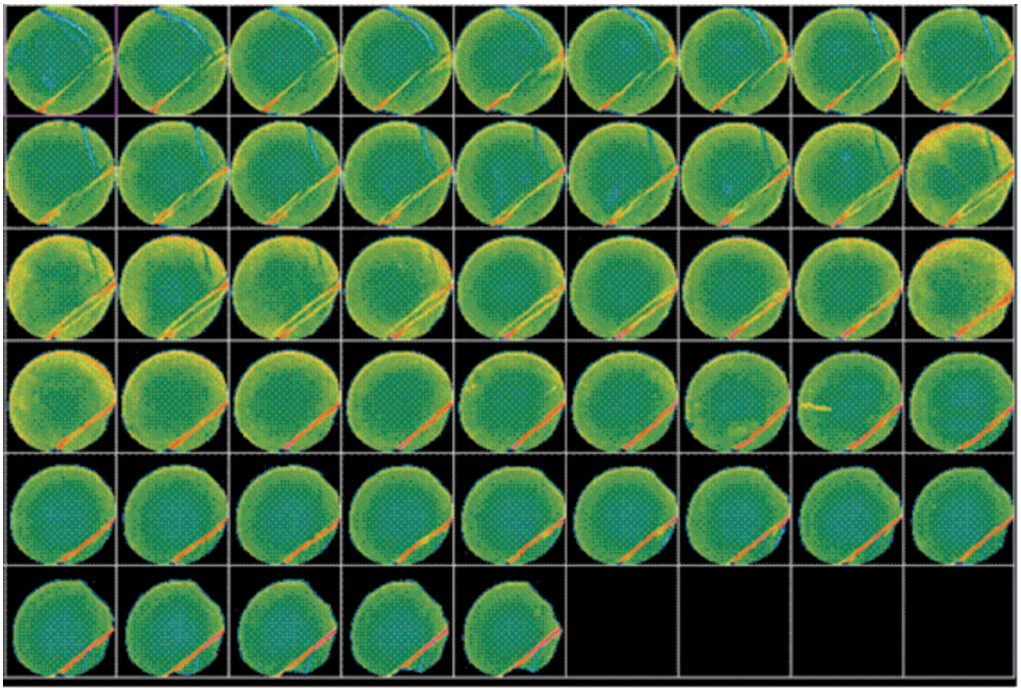

Fig. 12. CT images of Core-B

Rys. 12. Obrazy CT z rdzenia B

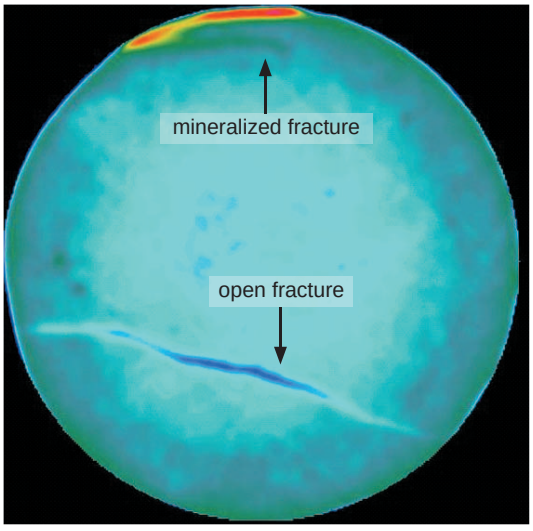

Fig. 13. Single CT image of Core-A.

Rys. 13. Pojedynczy obraz CT z rdzenia A

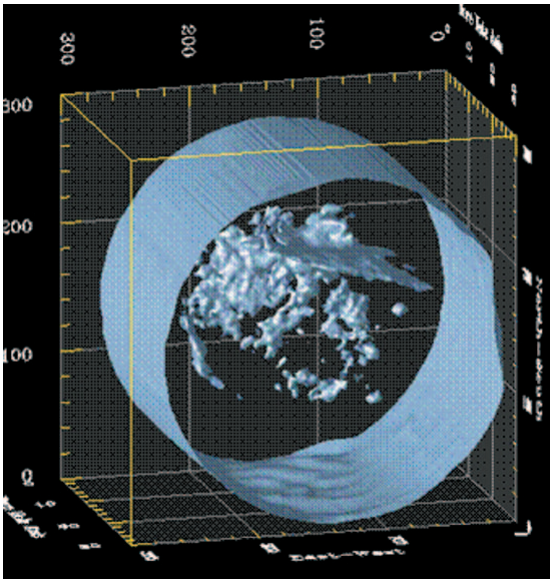

Fig. 14. 3-D image of fracture of Core-A

Rys. 14. Trójwymiarowy (3D) obraz szczeliny z rdzenia A

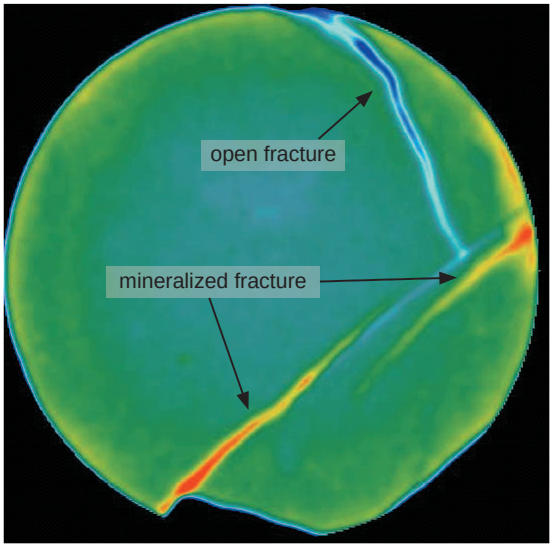

Fig. 15. Single CT image of Core-B

Rys. 15. Pojedynczy obraz CT z rdzenia B

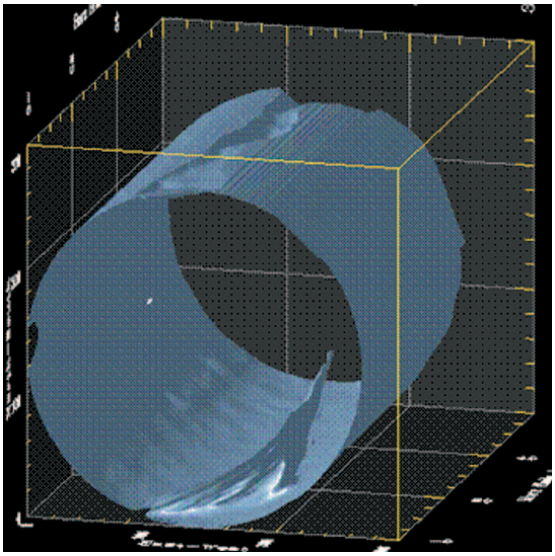

Fig. 16. 3-D image of fracture of Core-B

Rys. 16. Trójwymiarowy (3D) obraz szczeliny z rdzenia B

we generated the log normal distribution to fit the experimental data (Fig. 18). The generated value and the experimental data show a close agreement. This matching result confirms that the aperture distribution follows log-normal distribution. The matched values of statistical parameters are listed in Table 1. Fig. 19 shows the aperture distributions of both cores. The figure shows that the open fracture of Core-B is wider and distributes more evenly than the open fracture of Core-A. We also plotted the fracture aperture distribution of Core-A and Core-B in 2-D plane views as shown in Figs. 20 and 21, respectively. The results also confirm that the range of fracture aperture sizes of Core-A is much less than the size in Core-B since the open fracture in Core-B that extends to the outside of the core was probably caused by man-made induced fracture as mentioned earlier.

TABLE 1

Values of statistical parameters

TABLICA 1

Wartości parametrów statystycznych

	Mean [μm]	Standard Deviation [μm]
Core-A	222.17	577.50
Core-B	536.90	756.60

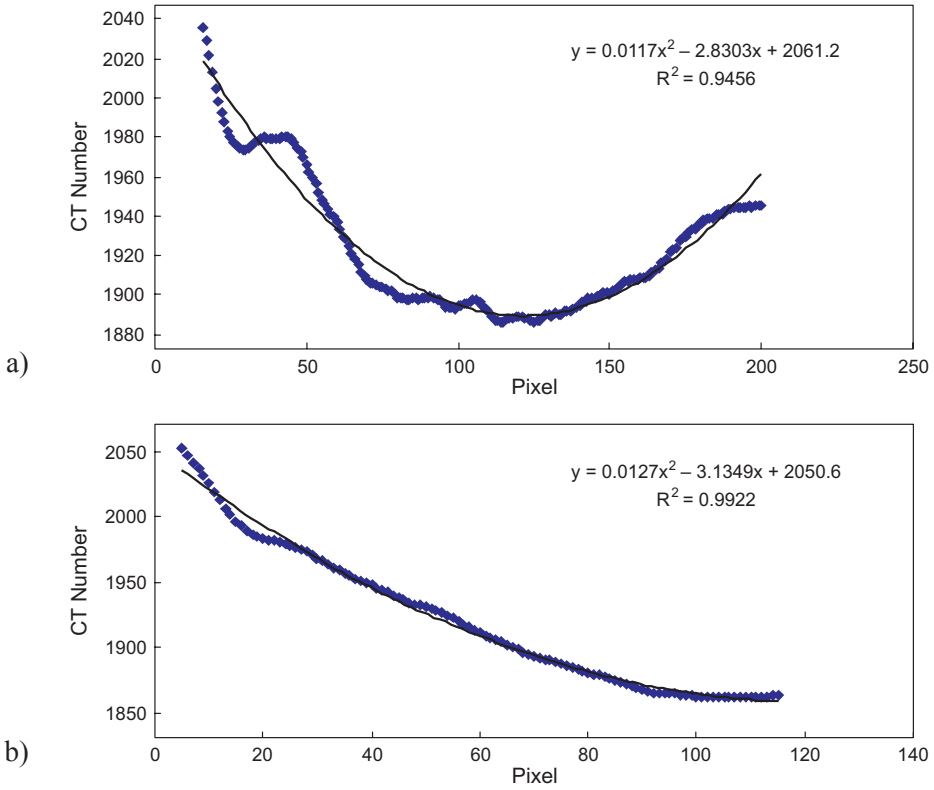

Fig. 17. Minimum CT number according to locations. a – Core-A, b – Core-B

Rys. 17. Określenie minimalnej liczby CT dla lokalizacji szczaliny. a – rdzeń A, b – rdzeń B

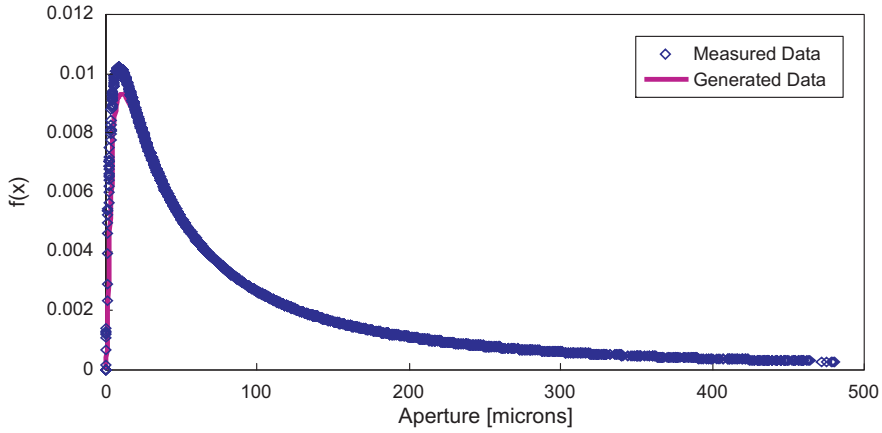

Fig. 18. Distribution of Measured Data & Generated Data (Core-A)

Rys. 18. Rozkład danych pomierzonych i wygenerowanych (rdzeń A)

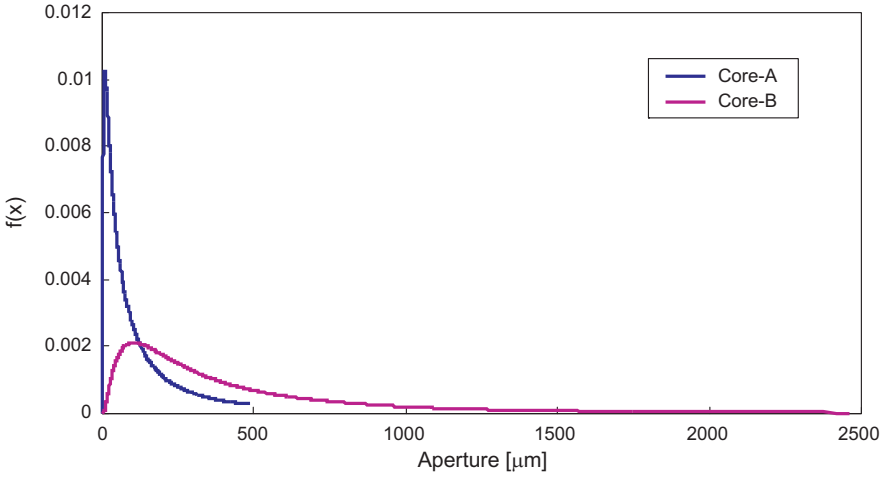

Fig. 19. Comparison of Aperture Distributions between Core-A and Core-B

Rys. 19. Porównanie rozkładu rozwarcia szczeliny pomiędzy rdzeniami A oraz B

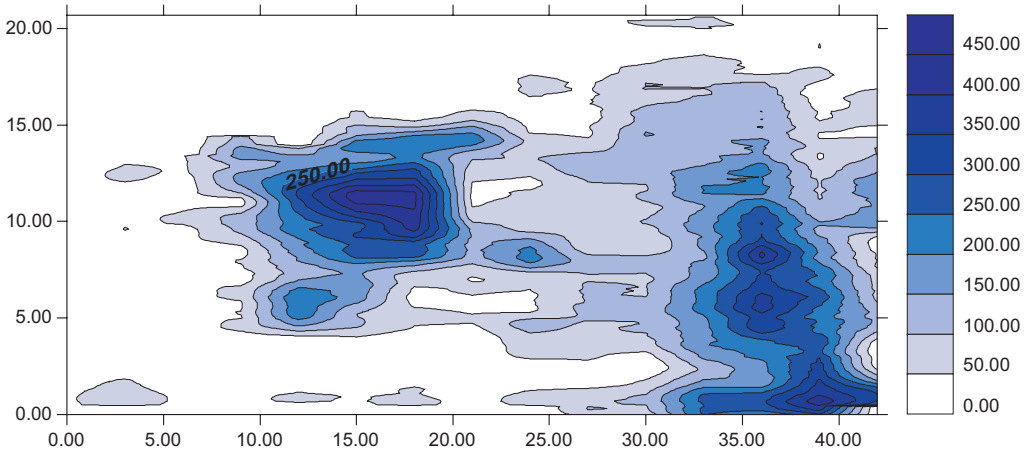

Fig. 20. Aperture contour map of Core-A in μm

Rys. 20. Mapa rozwarcia szczelin rdzenia A (w μm)

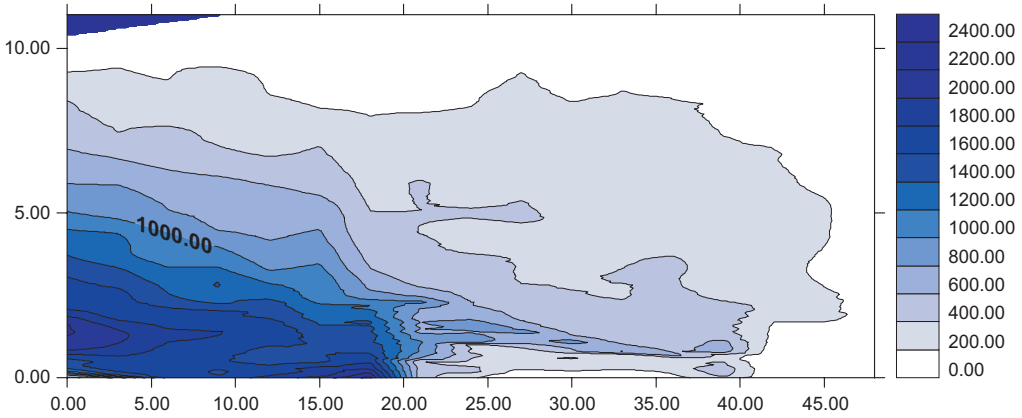

Fig. 21. Aperture contour map of Core-B in μm

Rys. 21. Mapa rozwarcia szczelin rdzenia B (w μm)

Conclusions

Based on this study, several conclusions can be derived as follows:

1. CT images taken from two RMOTC 48X28 cores show open fracture and mineralized fractures.
2. The measured fracture aperture distribution follows log-normal distribution.
3. The fracture aperture sizes and distribution from both cores are totally different. The aperture size of Core-B is bigger and more widely distributed than that of Core-A.
4. The fracture aperture contour maps of Core-A and Core-B clearly show preferential flow paths.
5. The fracture condition in Core-B is mainly affected by mineralization and induced fracture, meanwhile Core-A exhibits naturally fracture with limited mineral precipitation. Based on this condition, it is expected that the main flow path would occurs through Core-A.

Acknowledgement

The authors wish to thank the US Department of Energy (Project DE-FC26-01BC15361) for sponsoring this project.

REFERENCES

Putra E., Hidayati D., Schechter D.S., 2004. Reservoir Modeling of CO_2 Sequestration and Enhanced Oil Recovery in Teapot Dome. Project Narrative, U.S. DOE/NPTO Contract No. DE-PS26-04NT42249-1D (Oct. 5, 2004).

Lorenz J., Cooper S., 2004. Fractures in the Core from RMOTC 48X28 Core. Internal report to RMOTC, June 24, 2004.

Universal Systems Website (http://www.universal-systems.com/HD_350.asp).

Wellington S.L., Vinegar H.J., 1985. CT Studies of Surfactant-Induced CO_2 Mobility Control. paper SPE 14393 presented at the 1985 SPE Annual Technical Conference and Exhibition, Las Vegas, Sep. 22-25.

Muralidharan V., Chakravarty D., Putra E., Schechter D.S., 2004a. Investigating Fracture Aperture Distribution under Various Stress Conditions Using X-Ray CT Scanner. paper CIPC 2004-230 presented at 2004 Annual Technical Meeting of the Petroleum Society, Calgary, Canada, Jun. 8-10.

Muralidharan V., Chakravarty D., Putra E., Schechter D.S., 2004b. Simulation of Fluid Flow thorough Rough Fractures. paper SPE 89941 presented at the 2004 SPE International Petroleum Conference, Puebla, Mexico, Nov. 8-9.

Ang A., Tang W.H., 1975. Probability Concepts in Engineering Planning and Design. John Wiley & Sons.

Received: 02 February 2007